Real-Time Passive Acoustic Mapping With Enhanced Spatial Resolution in Neuronavigation-Guided Focused Ultrasound for Blood-Brain Barrier Opening

Supplementary Document

Sua Bae, Keyu Liu, Antonios N. Pouliopoulos, Robin Ji, and Elisa E. Konofagou

1. Passive Acoustic Mapping (PAM)

We compared the coherence-factor-based PAM (CF-PAM) with the conventional time-exposure-acoustics PAM (TEA-PAM)[1] and eigenspace-based robust Capon beamformer PAM (ERCB-PAM) [2]. For all methods (TEA, ERCB, and CF), the cavitation map was obtained by temporally integrating the intensity maps as follows:

$$\Psi(\mathbf{x}) = \sum_{t=1}^{N_t} I(\mathbf{x}, t)$$

where $I(\mathbf{x}, t)$ is the spatio-temporal cavitation intensity at the pixel $\mathbf{x}$ and the time point t where N_t is the number of time samples which is 100,000 for the 10-ms pulse with a sampling frequency of 10 MHz.

For TEA-PAM, the intensity was calculated as[1]

$$I_{\mathrm{TEA}}(\mathbf{x}, t) = \left| \sum_{i=1}^{N_E} \sqrt{d_i(\mathbf{x})} s_i\big(t + \tau_i(\mathbf{x})\big) \right|^2$$

where s_i is the acoustic signal received by the i-th element for a single burst, $d_i(\mathbf{x})$ is the distance between the pixel $\mathbf{x}$ and the i-th element, and $\tau_i(\mathbf{x})$ is the round-trip time delay, and N_E is the number of transducer elements.

For ERCB-PAM, the intensity was calculated as

$$I_{\mathrm{ERCB}}(\mathbf{x}, t) = \left| \sum_{i=1}^{N_E} w_{\mathrm{ERCB}}(i, \mathbf{x}) \sqrt{d_i(\mathbf{x})} s_i\big(t + \tau_i(\mathbf{x})\big) \right|^2$$

and $w_{\mathrm{ERCB}}(i, \mathbf{x})$ is the weight for the i-th channel at the pixel $\mathbf{x}$. The weight vector $\mathbf{w}_{\mathrm{ERCB}}$ for a certain pixel can be expressed as $\mathbf{w}_{\mathrm{ERCB}} = [w_1, w_2, \cdots, w_{N_E}]^{\mathrm{T}}$ and obtained by[2]

$$\mathbf{w}_{\mathrm{ERCB}} = \mathbf{U}_{\mathrm{S}} \mathbf{U}_{\mathrm{S}}^{T} \mathbf{w}_{\mathrm{RCB}}$$

where $\mathbf{U}_{\mathrm{S}}$ is the signal subspace which comprises the largest L eigenvalues. The signal subspace $\mathbf{U}_{\mathrm{S}} = [\mathbf{u}_1, \mathbf{u}_2, \cdots, \mathbf{u}_L]$ is obtained by the eigenvalue decomposition, $\mathbf{R} = \mathbf{U}\Lambda\mathbf{U}^T$, when $\mathbf{R}$ is the covariance matrix of the delayed signal, $\sqrt{d_i(\mathbf{x})} s_i\big(t + \tau_i(\mathbf{x})\big)$ where $i = 1, 2, \cdots, N_E$, integrated over all time points N_t. The L is determined by the parameter δ ($\delta < 1$) where $\lambda_1, \lambda_2, \cdots, \lambda_L > \delta \cdot \lambda_1$ and λ_1 is the largest eigenvalue[2]. $\mathbf{w}_{\mathrm{RCB}}$ is the data-adaptive weighting vector suggested by Coviello et al [3], which is also controlled by another user parameter ε.

2. GPU implementation of TEA- and ERCB-PAM

The computational speed of the proposed CF-PAM was compared with those of TEA- and ERCB-PAM[2]. For a fair comparison, TEA and ERCB were also implemented on GPU using parallel processing. For TEA-PAM, we used the same GPU realization scheme as CF-PAM (i.e., computing a spatial-temporal pixel per thread) except the calculation step for coherence factor. For the parallelization of ERCB-PAM, the covariance matrix calculation of delayed RF data was implemented on GPU. The calculation of weighting factors including eigenvalue decomposition was parallelized on multi-core CPU instead of GPU because it requires the eigenvalue decomposition process per pixel (i.e., per thread). The process speed was faster when it was implemented on a multi-core CPU than on the GPU because a CPU core can be more efficient than a GPU core for complex computations such as eigenvalue decomposition. The delay-and-sum process with the ERCB weighting factors was conducted by using GPU.

3. Cavitation Dose

We computed the stable cavitation dose with harmonic frequencies (SCDh), stable cavitation dose with ultraharmonic frequencies (SCDu), and inertial cavitation dose (ICD), as

$$\mathrm{SCDh} = \sqrt{\sum_{n=4}^{9} |P_{h,n}|^2}\,,$$

$$\mathrm{SCDu} = \sqrt{\sum_{n=4}^{9} |P_{u,n}|^2}\,,$$

$$\mathrm{ICD} = \sqrt{\sum_{n=4}^{9} |\bar{A}_n|^2}\,,$$

where $P_{h,n}$ and $P_{u,n}$ are the peak amplitude of the *n*-th harmonic and the *n*-th ultraharmonic frequency components, respectively, and $\bar{A}_n$ is the averaged amplitude over the bandwidth of 75 kHz between the *n*-th harmonic and the *n*-th ultraharmonic frequency. The peak amplitude was searched within the bandwidth of 1 kHz centered at each harmonic/ultraharmonic frequency. The frequency spectrum was obtained by summing the RF channel data across the elements and taking Fourier transform (number of points = 102,528, sampling frequency = 10 MHz). The frequency spectrum and the cavitation doses were obtained for every burst. Normalization was not applied for the cavitation dose calculation.

4. Simulation Data Generation for Spatial Resolution Evaluation

A 64-element phased array transducer with a center frequency (f_c) of 2.5 MHz and a pitch of 0.32 mm was assumed to passively receive harmonic signals from one or two cavitation sources.

For PSF evaluation, a cavitation source was located at the center of the array (x = 0) for the on-axis PSF or at x = 10 mm for the off-axis PSF evaluations. The depth of the cavitation source from the array transducer (z) was changed from 50 mm to 110 mm with an interval of 10 mm. For the source separation capability assessment, two cavitation sources are placed in the axial or lateral dimension. The distance between the two sources was 40, 50, or 60 mm in the axial direction (Δz) or 3, 4, or 6 mm in the lateral direction (Δx).

The harmonic signal emitted from the cavitation source was the sum of sinusoidal signals of the fundamental (f_c = 0.25 MHz) and the *n*-th harmonic (n = 2, ⋯, 16) frequencies with a duration of 1 ms. The simulated RF channel data were generated using the software package k-Wave [4] and MATLAB. Gaussian noise was added to the RF data to have a signal-to-noise ratio of 10 dB and the impulse response of the transducer was convoluted to get the bandlimited data assuming the −6 dB transducer bandwidth of 70% with a center frequency of 2.5 MHz. The bandlimited data were then downsampled to 10 MHz which is four times the center frequency. Data were zero-padded to take into account the initial transmit delay which corresponds to the distance from the FUS transducer to the cavitation source.

5. MRI

Prior to the treatment, the animal with fiducial markers was scanned for the anatomical registration with the neuronavigator (T1-weighted, TR/TE = 7.4/3.1 ms, FA = 11°, resolution = 0.4 × 0.4 × 0.8 mm^3; SIGNA Premier 3-T, GE Medical Systems, USA). Before and after the treatment, contrast-enhanced T1-weighted images were acquired with the same MR sequence with the gadolinium-based agent (0.2 mL/kg; Omniscan, GE Healthcare, USA) for the BBB opening confirmation and quantification. The scans before the treatment were used as the baseline. T2-weighted, susceptibility-weighted, diffusion-weighted, and apparent diffusion coefficient MRI were also obtained as safety scans to detect acute edema or hemorrhage after the FUS.

Post-FUS MRI was obtained approximately 2 hours after treatment and the contrast agent was injected 30 min before the T1-weighted scan. For BBB opening quantification, the baseline MRI was subtracted from the post-FUS MRI which was registered to the baseline MRI. The BBB opening volume was identified by thresholding the intensity of the subtracted MRI. The threshold was chosen such that the mean intensity of the identified volume whose pixel intensities are higher than the threshold ($\bar{I}_{\mathrm{bbbo}}$) is significantly higher than the mean intensity of background surrounding pixels ($\bar{I}_{\mathrm{bkg}}$) with a confidence level of 99% (i.e., $\bar{I}_{\mathrm{bbbo}} - \bar{I}_{\mathrm{bkg}} > 2.58\sigma_{\mathrm{bbbo+bkg}}$ when $\sigma_{\mathrm{bbbo+bkg}}$ is the standard deviation of the intensity of both regions assuming a Gaussian distribution of the pixel intensity).

The MRI volume was registered with the ultrasound images (B-mode and PAM) based on the coordinates and directional vectors of the ultrasound transducer obtained from the neuronavigation system, and the B-mode image was employed to compensate for the marginal registration errors (~5 mm) from the neuronavigation system by using the anatomical landmarks. To obtain a 2-D BBB opening map in good agreement with 2-D PAM image, we selected a slice with a 10-mm thickness at the corresponding spatial slice in the MR volume, considering the elevational slice thickness of the array transducer for PAM. The volume was then summed along the elevational direction, resulting in a 2-D map of BBB opening which was used for the ROC study with the 2-D cavitation map.

6. Off-axis Point Spread Function (PSF) Size

Point spread function (PSF) size was also measured for the off-axis source positions using the simulated data. Data were obtained as described in IV.A and the cavitation sources were placed at x = 10 mm, z = 50, 60, ⋯, 110 for the off-axis PSF investigation. As shown in Fig. S1, off-axis PSF is tilted toward the center of the receive array, which is the origin (x=0, z=0) of the coordinate system. The axial length was measured along the line that passes the origin (x=0, z=0) and the source location, and the width of PSF was measured along the perpendicular line to the axial line of the PSF. As the on-axis PSF comparison results (Fig. 3(a)–(d)), the off-axis comparison (Fig. S1(b) and (c)) also showed that the PSF size of CF-PAM was similar to that of ERCB-PAM and smaller than that of TEA-PAM.

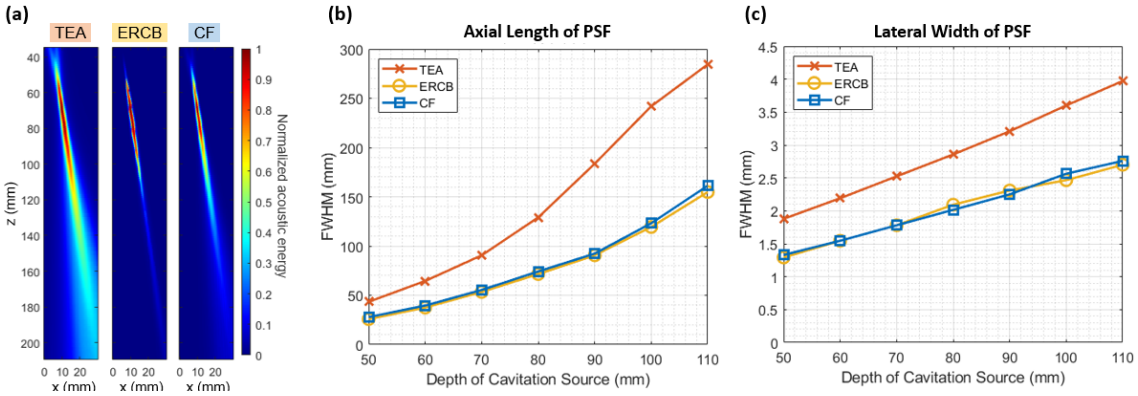

Fig. S1. (a) Off-axis point spread functions (PSFs) of TEA-, ERCB-, and CF-PAM obtained from a single cavitation source at x = 10 mm, z = 70 mm. (b), (c) Full-width half-maximum (FWHM) of PSFs in (c) the axial and (d) the lateral direction for the point sources at x = 10 mm, z = 50, 60, ⋯, 110.

7. Parallel processing speed comparison with other studies

Although the real-time realization of full-burst CF-PAM with the neuronavigation-guided FUS system was presented for the first time herein, prior studies have been reported on GPU-based full-burst PAM with different FUS setups. Lyka et al. [5] presented the GPU processing of RCB-PAM at a rate of 1 Hz (N_E = 128; N_p = 660; N_t = 2,000), where N_E, N_p, and N_t represent the number of channels (or receiving elements), pixels, and time samples, respectively. Jones et al. reported the online processing at a rate of 1 Hz (N_E = 256; N_p = 11 × 11 × 11 = 1,331; N_t = 30,000) in [6], and at 0.45 Hz for 4 targets (N_E = 256; N_p = 11 × 11 × 21 = 2,541; N_t = 30,000) in [7]. Adams et al. also published their work with the online cavitation mapping at a rate of 0.67 Hz for 4-point sonication (N_E = 64; N_p = 11 × 11 × 15 = 1,815; N_t = 100,000 [8]. The processing time per channel, pixel, sample, and target in the previously published literature ranged from 5.9×10^{-9} s [5] to 2.8×10^{-11} s [7], while our processing time presented herein was 5.5×10^{-12} s. However, a direct comparison with these realizations might not be appropriate because the different GPUs and hardware were used, the PAM methods employed were also different, and some studies included the overhead time in the processing time reported [6]–[8].

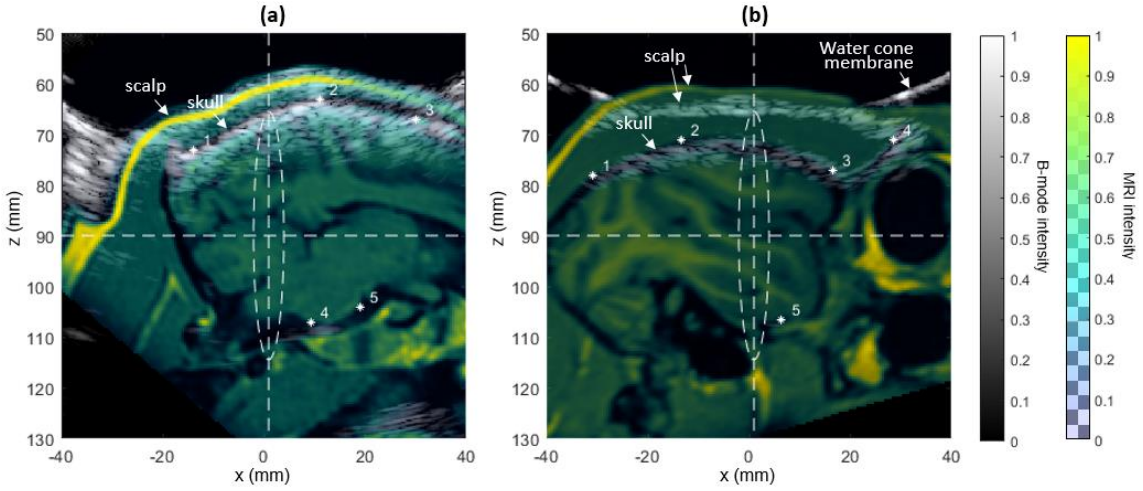

Fig. S2. Co-registration of ultrasound B-mode image (gray) and MRI (color) for (a) NHP 1 and (b) NHP 2. The registration was based on the transformation matrix from the neuronavigation system and the minor correction was manually performed based on the landmarks (asterisks) at the skull bone. The hyper-echoic skull in B-mode was matched with the hypo-intense region in MRI for both NHPs. The mismatch at the scalp in NHP 2 was due to the compression of the thick muscle tissue (hypo-echoic in B-mode) at the anterior part of the head by the weight of the water in the B-mode image which was captured during the FUS treatment; on the other hand, the MRI was obtained separately in the MR scanner without the compression.

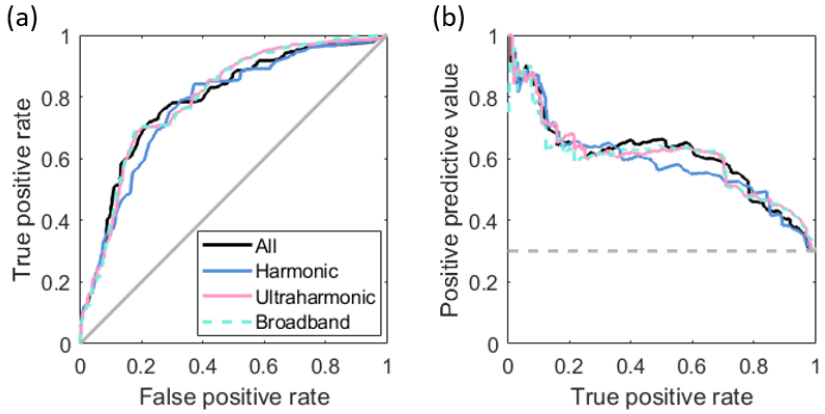

Fig. S3. (a) ROC and (b) PR curves for pixel-wise prediction of BBB opening in NHP with the PAM intensity of cavitation maps reconstructed from all, harmonic, ultraharmonic, and broadband frequency components. AUC_{ROC} was 0.790, 0.775, 0.796, and 0.796, and AUC_{PR} was 0.608, 0.590, 0.604, and 0.598 for all, harmonic, ultraharmonic, and broadband frequency bands. Frequency-selective cavitation maps did not significantly enhance the spatial correlation between the PAM intensity and the gadolinium enhancement in MRI.

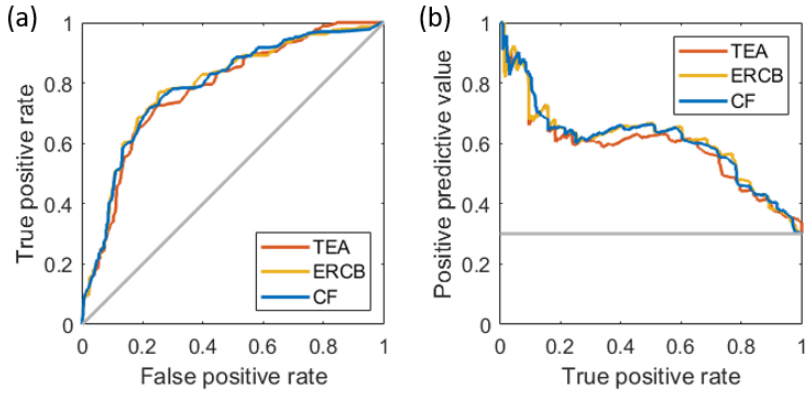

Fig. S4. (a) ROC and (b) PR curves for in vivo NHP pixel-wise binary classification of BBB opening with the PAM intensity obtained by TEA, ERCB, and CF methods. The ROC analysis was performed by combined data sets from NHP 1 and NHP 2. AUC_{ROC} was 0.779, 0.791, and 0.790 AUC_{PR} was 0.588, 0.608, and 0.608 for TEA, ERCB, and CF, respectively. Despite the better spatial resolution of CF-PAM and ERCB-PAM compared to TEA-PAM, the prediction capability of BBB opening was marginally enhanced (1.5% and 3.4% for AUC_{ROC} and AUC_{PR}).

References

[1] M. Gyöngy and C. C. Coussios, "Passive spatial mapping of inertial cavitation during HIFU exposure," *IEEE Transactions on Biomedical Engineering*, vol. 57, no. 1, pp. 48–56, 2010.
[2] S. Lu, H. Hu, X. Yu, et al., "Passive acoustic mapping of cavitation using eigenspace-based robust Capon beamformer in ultrasound therapy," *Ultrasonics Sonochemistry*, vol. 41, pp. 670–679, 2018.
[3] C. Coviello et al., "Passive acoustic mapping utilizing optimal beamforming in ultrasound therapy monitoring," *J. Acoust. Soc. Am.*, vol. 137, no. 5, pp. 2573–2585, 2015.
[4] B. E. Treeby, J. Jaros, A. P. Rendell, and B. T. Cox, "Modeling nonlinear ultrasound propagation in heterogeneous media with power law absorption using a k-space pseudospectral method," *J. Acoust. Soc. Am.*, vol. 131, no. 6, pp. 4324–4336, 2012
[5] E. Lyka, C. M. Coviello, C. Paverd, M. D. Gray, and C. C. Coussios, "Passive acoustic mapping using data-adaptive beamforming based on higher order statistics," IEEE Trans. Med. Imaging, vol. 37, no. 12, pp. 2582–2592, 2018.
[6] R. M. Jones, L. Deng, K. Leung, D. McMahon, M. A. O'Reilly, and K. Hynynen, "Three-dimensional transcranial microbubble imaging for guiding volumetric ultrasound-mediated blood-brain barrier opening," Theranostics, vol. 8, no. 11, pp. 2909–2926, 2018.
[7] R. M. Jones, D. McMahon, and K. Hynynen, "Ultrafast three-dimensional microbubble imaging in vivo predicts tissue damage volume distributions during nonthermal brain ablation," Theranostics, vol. 10, no. 16, pp. 7211–7230, 2020.
[8] C. Adams et al., "Implementation of a skull-conformal phased array for transcranial focused ultrasound therapy," IEEE Trans. Biomed. Eng., vol. 68, no. 11, pp. 3457–3468, Nov. 2021.